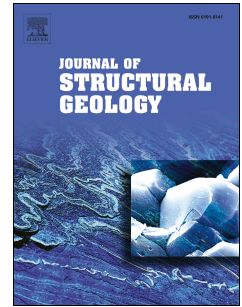


# Accepted Manuscript

Microfracture spacing distributions and the evolution of fracture patterns in sandstones

J.N. Hooker, S.E. Laubach, R. Marrett



PII: S0191-8141(17)30072-X

DOI: [10.1016/j.jsg.2017.04.001](https://doi.org/10.1016/j.jsg.2017.04.001)

Reference: SG 3468

To appear in: *Journal of Structural Geology*

Received Date: 23 November 2016

Revised Date: 20 March 2017

Accepted Date: 2 April 2017

Please cite this article as: Hooker, J.N., Laubach, S.E., Marrett, R., Microfracture spacing distributions and the evolution of fracture patterns in sandstones, *Journal of Structural Geology* (2017), doi: 10.1016/j.jsg.2017.04.001.

This is a PDF file of an unedited manuscript that has been accepted for publication. As a service to our customers we are providing this early version of the manuscript. The manuscript will undergo copyediting, typesetting, and review of the resulting proof before it is published in its final form. Please note that during the production process errors may be discovered which could affect the content, and all legal disclaimers that apply to the journal pertain.

**Microfracture spacing distributions and the evolution of fracture patterns in sandstones**J.N. Hooker<sup>\*1,2,3</sup>S.E. Laubach<sup>2</sup>R. Marrett<sup>2</sup>

1. Department of Earth Sciences, University of Oxford, South Parks Road, Oxford, OX1 3AN, UK.

2. Bureau of Economic Geology, Jackson School of Geosciences, The University of Texas at Austin,  
10100 Burnet Road Bldg. 130, Austin, Texas, 78758.

3. Department of Geological Sciences, Jackson School of Geosciences, The University of Texas at  
Austin, 2305 Speedway, Stop C1160, Austin, TX 78712.

\*Corresponding author; john.hooker@earth.ox.ac.uk.

Keywords: Microfracture, fracture spacing, sandstone, SEM-CL, diagenesis

Microfracture spacing distributions and the evolution of fracture patterns in sandstones

J.N. Hooker\*<sup>1,2,3</sup>

S.E. Laubach<sup>2</sup>

R. Marrett<sup>2</sup>

1. Department of Earth Sciences, University of Oxford, South Parks Road, Oxford, OX1 3AN, UK.

2. Bureau of Economic Geology, Jackson School of Geosciences, The University of Texas at Austin,  
10100 Burnet Road Bldg. 130, Austin, Texas, 78758.

3. Department of Geological Sciences, Jackson School of Geosciences, The University of Texas at  
Austin, 2305 Speedway, Stop C1160, Austin, TX 78712.

\*Corresponding author; john.hooker@earth.ox.ac.uk.

## Abstract

Natural fracture patterns in sandstone were sampled using scanning electron microscope-based cathodoluminescence (SEM-CL) imaging. All fractures are opening-mode and are fully or partially sealed by quartz cement. Most sampled fractures are too small to be height-restricted by sedimentary layers. At very low strains ( $< \sim 0.001$ ), fracture spatial distributions are indistinguishable from random, whereas at higher strains, fractures are generally statistically clustered. All 12 large ( $N > 100$ ) datasets show spacings that are best fit by log-normal size distributions, compared to exponential, power law, or normal distributions. The clustering of fractures suggests that the locations of natural fractures are not determined by a random process. To investigate natural fracture localization, we reconstructed the opening history of a cluster of fractures within the Huizachal Group in northeastern Mexico, using fluid inclusions from synkinematic cements and thermal-history constraints. The largest fracture, which is the only fracture in the cluster visible to the naked eye, among 101 present, opened relatively late in the sequence. This result suggests that the growth of sets of fractures is a self-organized

process, in which small, initially isolated fractures grow and progressively interact, with preferential growth of a subset of fractures developing at the expense of growth of the rest. Size-dependent sealing of fractures within sets suggests that synkinematic cementation may contribute to fracture clustering.

## 1. Introduction

The spacing of natural fractures is a well studied problem, in part because fracture spacing controls the probability of fracture intersection during tunneling or drilling (Narr, 1996). Statistics that can describe useful aspects of fracture spacing include the mean, which governs the overall expected frequency of fracture intersection, as well as the standard deviation, which describes the spatial regularity of the fractures. That is, a hypothetical fracture set may be perfectly regularly spaced, or highly clustered, with statistically random spacing occupying an intermediate position on the spatial regularity spectrum (Gillespie et al., 1999).

In the present study we focus on the spacing of opening-mode fractures that are fully or partially filled by mineral cements. In doing so we restrict our attention to fractures that demonstrably formed in the subsurface. As well, we can use mineral cements to support a genetic link between fractures in a geologic setting (Smith et al., 2014) and, in certain cases, to constrain the timing and fluid conditions of fracture opening (e.g., Becker et al., 2010). We discuss how our findings might also apply to the spacing of other types of fractures, such as magmatic dykes and barren fractures.

Geologic fractures are generally thought to initiate at flaws, based on the experimental work of Griffith (1921) as well as field evidence that large joints propagated from small joints located at fossils or sedimentary structures (e.g., Helgeson and Aydin, 1991; Savalli and Engelder, 2005). As such, the spacing of large fractures could reflect the spacing of flaws. However, it is commonly assumed that flaws are randomly dispersed throughout the host rock (e.g., Olson, 1993; Tang et al., 2008). The challenge in explaining fracture patterns, then, is how to start from an unorganized flaw distribution and produce a non-random pattern?

Regular spacing is commonly observed in stratified rocks (e.g., Ladeira and Price, 1981; Narr and Suppe, 1991). In such cases, fracture growth is commonly height-restricted and fracture spacing scales with the height of fractures, resulting in a periodic fracture spacing (Schöpfer et al., 2011). However, many highly clustered, and demonstrably non-random, fracture patterns have been identified, both in stratabound and non-stratabound fracture sets (see literature review in Hooker and Katz, 2015).

Various explanations of clustering have been proposed. Fractures can cluster in the vicinity of folds (Ogata et al., 2014) or faults (Putz and Sanderson, 2008). Diagenetic processes can create brittle zones that become preferentially fractured (Giorgioni et al., 2016). Sedimentary fabrics can be laterally anisotropic and produce spatially variable fracture patterns (Ogata et al., 2016). Finally, swarms of joints in the vicinity of magmatic dykes were attributed to tensile stresses related to dyke propagation (Delaney et al., 1986). This last example highlights the potential for fracture clustering to develop dynamically, during propagation, and therefore be inherent to fracture strain accumulation.

Furthermore, fractures visible to the naked eye (macrofractures) are commonly surrounded by microscopic fractures (microfractures), such that the largest fractures are bedding-bound and the smaller ones are not (Hooker et al., 2013). Consequently, even uniformly spaced, bedding-bound fracture patterns may have emerged from fracture growth that was initially unaffected by mechanical stratification.

With the goal of testing the relative importance of flaw distributions, sedimentary features, structures, and self-organization to the development of natural fracture patterns, this study presents microfracture spacing measurements, compiled from eight formations on three continents. The same data collection method was uniformly employed, over the same scale of observation, so that data can be compared over a range of structural settings. Fractures were measured in sandstones observed using SEM-CL, at a scale that we argue is sufficiently small to preclude height-restriction of most fractures by

mechanically significant sedimentary bed boundaries. We perform statistical tests for the observed spacings to test whether natural microfractures are more or less clustered than would be predicted by a random arrangement of fractures.

To further investigate the processes that control fracture spacing, we examine the timing of opening of a cluster of fractures within the Triassic El Alamar Formation (Huizachal Group) of northeast Mexico, which is one of our sampling locations, using fluid-inclusion microthermometry and thermal history modeling. This study is the first that we know of to present independent timing evidence for a group of parallel, co-genetic fractures. We compare our results to previous models of fracture propagation and find support for previous theoretical models in which fracture clustering is the result of dynamic crack interaction during propagation.

## 2. Methods

The microfracture spacing dataset was assembled using rock samples collected from sandstones containing natural macrofractures (Table 1). Macrofracture patterns were observed either in core or in outcrop. Fracture spacing is defined as the distance between neighboring fractures, measured perpendicular to the fractures, along a single line of observation (scanline). In each sandstone the macrofractures are present in sub-parallel sets; typically strike dispersion is less than 20° at a single locality, unless multiple, consistently crosscutting sets are present. In the latter case, microfracture orientations and crosscutting relationships reflect those of the macrofractures, and distinct sets were analyzed separately. Fractures in parallel sets are all observed to have the same mineral-fill sequence, as described below.

### \*TABLE 1\*

At outcrop or within core, fracture spacings were observed using a 10× hand lens. For each macrofractured sandstone we collected one or more samples for microfracture analysis. Microfracture

samples were collected as close to the macrofracture scanline as possible. Layer-parallel thin sections were cut in order to construct microfracture scanlines parallel to the macrofracture scanlines.

In this study we examine and interpret the variation in fracture spacing and strain, as measured along 1D scanlines. It is important to note that we are rarely able to observe fracture patterns in 3D, and have made no 3D analyses. Because our measurements have been made across fractures and in map-view, our methods are most applicable to problems such as fracture intersection while drilling along bedding. If drilling across bedding, our observations could help to assess whether a fracture will be intersected at the horizon of interest. On the other hand, vertically stacked fracture patterns, as might be anticipated among buoyancy-driven fractures such as magmatic dykes or sandstone intrusions, would be difficult to evaluate using our technique.

Thin sections were carbon-coated and imaged using an Oxford Instruments MonoCL2 cathodoluminescence detector attached to an FEI XL30 scanning electron microscope. A working distance of 10 mm was used, which is the smallest possible working distance compatible with our CL mirror. As we explain below, the ambiguous origin of intragranular fractures served as the *de facto* lower size-limit of our fracture-mapping capability. Consequently, imaging was optimized for signal and areal coverage, as opposed to resolution, by using a 15 kV beam voltage, 150× magnification (pixel width 0.77  $\mu\text{m}$ ) and a large spot size.

Individual digital SEM-CL images were stitched together using Photoshop. Fractures were then interpreted, and spacings measured, along scanlines drawn on stitched mosaics using the mapping program Didger. Measurements were automatically extracted using an Excel routine (Gomez and Laubach, 2006) that trigonometrically corrects spacings to reflect the fracture-perpendicular distance between neighboring fractures.

Thermometric fluid inclusion measurements were performed using a FLUID, INC.-adapted, USGS-type, gas-flow heating/freezing stage. The thermometer was calibrated using the CO<sub>2</sub>-ice melting

temperature ( $T_m$ ) at  $-56.6^\circ\text{C}$  of  $\text{H}_2\text{O}-\text{CO}_2$  synthetic fluid inclusions, the ice  $T_m$  at  $0^\circ\text{C}$ , and the critical homogenization temperature ( $T_h$ ) at  $374.1^\circ\text{C}$  of pure  $\text{H}_2\text{O}$  synthetic fluid inclusion standards (Sterner and Bodnar, 1984).

### 3. Sample suite and fracture description

The sandstones studied reflect a variety of structural settings (Table 1). Each geologic setting was described in the Appendix of Hooker et al. (2014), which demonstrated that the aperture-size distributions of most individual datasets are well fit by power laws. Sandstones were selected for study based on the presence of one or more sets of fractures, identified as natural and reflecting geological processes by the presence of mineral cements that line or fill fractures.

Most scanlines were drawn across exposures of massive sandstones that bear fractures not strongly bound to individual layers (Table 1). Exceptions to this are most scanlines from the Piceance and East Texas basins, which have very low strain and abundant mud-rich beds that generally served as barriers to fracture propagation. In general, fracture strain reflects the extent of regional tectonic deformation, with low strain in regional arches having gentle curvature, and high strain in mountain belts (Table 1). Note that all strain measurements reported here are fracture strain measurements, which are calculated from scanline data as the sum of apertures divided by the sum of spacings. This measurement therefore does not include penetrative strain or any other deformation, related or unrelated to the fracture-generating event.

Petrographic imaging of a representative suite of samples shows that essentially all samples contain quartz cement lining the fracture walls. Quartz may seal fractures entirely or may be overlapped by pore space, carbonate cements, or, rarely, hydrocarbons or clay. Within a given fracture set, larger fractures are less likely to be completely sealed by quartz cement (Fig. 1D). Quartz cement commonly contains crack-seal texture (Fig. 1B), indicating repeated increments of opening and sealing within each fracture. Carbonate cements rarely contain crack-seal texture.

\*FIGURE 1\*

Microfractures observed under SEM-CL can commonly be reconstructed via the offset of grains along fracture walls (Fig. 1A, C). The microfractures surveyed here generally have purely opening displacement. The vertical orientation of macrofractures, and the absence of any brecciation, slickensides, or offset bedding suggest that the macrofractures likewise are dominantly opening-mode. Fracture walls are discrete and generally smooth and planar at the outcrop scale (Fig. 1E). However, fractures are locally discontinuous; fracture traces commonly splay into en échelon segments (Fig. 1A, E) and may deviate at grain boundaries (Fig. 1A).

Although fracture length was not measured for most samples in this study, systematic fracture-length surveys from maps assembled of SEM-CL images from a subset of our sampling localities indicate roughly square-root scaling of aperture to length (Figure 2). Microfractures having apertures in the range of 5-25  $\mu\text{m}$  have lengths on the order of 200-4000  $\mu\text{m}$ . Because beds sampled are typically at least decimeters thick, we infer that most microfractures observed in this study are not layerbound, although some control on microfracture propagation may be exerted at the crossbed scale or, as described below, the grain scale.

\*FIGURE 2\*

SEM-CL imaging reveals abundant microfractures encased entirely within individual quartz grains (Fig. 1A). Such microfractures may reflect brittle deformation predating the deposition of the quartz grain into the sandstone under investigation, and so may be unrelated to fractures that formed after deposition of the sandstone (Laubach, 1997).

In contrast, transgranular microfractures (Fig. 1A, C, D) demonstrably formed within the rock after grain deposition. Transgranular microfractures were detected using SEM-CL in all samples, except

two samples from relatively short scanlines through low-strain rocks (Table 1, 2). For this analysis we calculate fracture spacing between transgranular fractures, ignoring intragranular fractures. In principle, some intragranular fractures are probably genetically related to the transgranular ones, and therefore our spacings are wider than the true spacings between microfractures. However, for the intragranular microfractures, no CL color or texture criteria could be used to identify a subpopulation of microfractures running parallel to the macrofractures, nor did the populations of intragranular microfractures have preferred orientations. In contrast, the transgranular fractures are invariably present in parallel sets striking parallel to macrofractures. Therefore, we did not include intragranular microfractures in our analysis.

\*TABLE 2\*

Furthermore, crack-seal increment sizes have a finite thickness that is resolvable using 150× magnification (Hooker et al., 2014), typically on the order of 5–10 µm. Where isolated, such increments commonly transgress multiple grains. We therefore interpret that the sedimentary granularity of sandstones is probably mechanically significant for natural fracture scaling, perhaps because the flaws from which fractures nucleate correspond to weak grain boundaries, clay fragments, or grain-scale pores. Brittle deformation likely also occurs at the subgranular scale (Anders et al., 2014), but the granular texture of the host rock for the scale at which such processes occur compel us to ignore them for the present study, as we are limiting our analysis to transgranular microfractures.

We collected samples for fluid-inclusion analysis from the Triassic El Alamar sandstone (Huizachal Group) in the Sierra Madre Oriental of northeast Mexico. This field setting permitted a study of the spatial and temporal accrual of fracture strain because of several key factors. First, the outcrop exposes four clearly defined fracture sets in plan view. Second, synkinematic quartz cements within fractures preserve fluid inclusions from which homogenization temperatures can be reliably measured. Third, independent burial-history investigations have constrained the thermal history of the study area, so that the timing of fracture opening can be inferred based on fluid-inclusion

temperatures. Using these fractures we investigated the sequence of opening of parallel fractures and therefore the evolution of a fracture set's spatial arrangement.

#### 4. Spacing data

Fracture strain, calculated as (sum of apertures)/(sum of spacings), ranges from  $1 \times 10^{-4}$  to  $2 \times 10^{-1}$  (Tables 1, 2). As detailed above, scanlines were drawn across vertical core samples, slant-core samples, and outcrop exposures, and so range in length from 20 to 2067 mm. Longer scanlines provide more robust sampling statistics, and are particularly important for analyzing low-strain, widely spaced fracture sets.

We quantified the irregularity of fracture spacing using the coefficient of variation,  $C_v$  (e.g., Gillespie et al., 1999), calculated as  $\sigma/\mu$ , where  $\sigma$  is the standard deviation of fracture spacings and  $\mu$  is the mean. Thus a perfectly periodic fracture spacing will produce a  $C_v$  of zero, and  $C_v$  will increase with increasing irregularity of spacing. Assigning random locations to hypothetical fractures produces a  $C_v$  near 1 (Fig. 3A). In order to test the null hypothesis that an observed natural fracture sequence is randomly distributed, we derived 95% confidence intervals to  $C_v$  values for random fracture locations. The values were created by generating N (5–300) random fracture locations 1000 times, using the resulting 5<sup>th</sup> and 95<sup>th</sup> percentile  $C_v$  values as the critical values, outside of which we reject the null hypothesis.

**\*FIGURE 3\***

We quantified the heterogeneity of fracture strain using the  $V'$  statistic of Kuiper (1960), applied to fractures by Putz and Sanderson (2008). For this statistic, the cumulative aperture at each fracture is compared to a line of homogeneous strain; i.e., what the cumulative aperture would be at that point if the strain were homogeneously distributed (Fig. 4A). This difference is called  $D_{\max}$  where it is most positive and  $D_{\min}$  where it is most negative.  $V'$  is calculated as  $(|D_{\max}| + |D_{\min}|)/A$ , where A is the total

cumulative aperture.  $V'$  is therefore a measure of the strain heterogeneity within the scanline. Perfectly regular fracture spacing will produce a  $V'$  approaching zero as fracture size decreases. The maximum possible strain heterogeneity is all strain manifest within a single fracture, which would produce  $V' = 1$  if the fracture lies at the beginning or end of the scanline. Stephens (1965) tabulated upper- and lower-tail critical values for the significance of  $V'$  against the null hypothesis that measurements come from a hypothesized distribution, which in our case is a uniform distribution. Fracture strain patterns that fall below or above the critical values given by Stephens (1965) can be interpreted as more homogeneous or more clustered, respectively, than would be expected from a random fracture strain distribution.

\*FIGURE 4\*

Best-fit equations to each spacing population can be compared using the  $\chi^2$  statistic (e.g., Hooker et al., 2014). A  $\chi^2$  test, in which the  $\chi^2$  statistic for the observed spacings is compared to a hypothetical population following the corresponding equation, allows rejection of the proposed equation with a given level of confidence (e.g., McKillup and Dyar, 2010).

## 5. Interpretation of spacing statistics

No datasets has  $C_v$  significantly less than expected for random fracture locations (Fig. 3A), hence we do not interpret any datasets as regularly or periodically spaced. Furthermore, only three datasets, having  $N = 3, 4$ , and  $6$ , have  $V'$  lower than the lower-tail critical value for a uniform distribution (Table 2, Fig. 4B), for which we would interpret homogeneously distributed fracture strain. Of 60 total datasets, 39 exceed the critical value for either (18) or both (21) regular fracture spacing tests,  $C_v$  and  $V'$  (Table 2). From these results we infer that the measured fracture spacings are either indistinguishable from random or systematically clustered.

Furthermore, we note that the samples with the greatest numbers of fractures are most commonly distinguishable from random patterns. This relationship could reflect increasing spatial heterogeneity of the fracture pattern with increasing strain. Alternatively, this pattern may be a statistical artifact, because it may be that low-strain samples are also non-randomly distributed, but that limited sampling of low-strain fracture sets makes distinguishing such patterns from random more difficult.

One way to distinguish between these two possibilities is to examine the few long scanlines through low-strain fracture sets. The best such example is Sample 41. This scanline is more than a meter long and intersects 20 microfractures. The sampled fractures are indistinguishable from random, using both  $C_v$  and  $V'$ . Of 37 datasets having as many or fewer fractures, 17 are distinguishable from random by one or both measures. The example of Sample 41 therefore supports the interpretation that low-strain fracture sets are randomly distributed, in terms of spacings along scanlines.

Another approach is to interrogate the low-N datasets in aggregate. If some non-random spatial-organization process were active during the initiation of fracture sets, then although each low-N set is poorly sampled, we might nonetheless expect that non-random signal to be detected within some low-N sets. Instead, we observe that  $C_v$  is consistently indistinguishable from random for low-N sets and that  $C_v$  increases with increasing fracture abundance (fractures per mm, Fig. 3B). This correlation is stronger than that between  $C_v$  and number of fractures (Fig. 3A), presumably reflecting an increase in fracture clustering with fracture abundance, and not just dataset quality.

## 6. Reconstructing a natural fracture array

Four sets of fractures are present in a canyon exposure of the Huizachal Group (Figure 5). Each set comprises strike-parallel, steeply dipping, quartz- and calcite-cemented fractures. The relative timing of these four sets was constrained using crosscutting relationships by Laubach and Ward (2006), who labeled the sets A (earliest) through D (latest). Sample 44 of the fracture spacing dataset was measured from Set C at this location. Preliminary fluid-inclusion thermometry data in Laubach and

Ward (2006), and detailed fluid-inclusion data combined with SEM-CL imaging (Hooker et al., 2015) were used to constrain the timing of each fracture set with respect to the regional burial history. This burial history (Fig. 5D) was modeled using K-Ar dating of diagenetic illite, regional fluid inclusion thermometric data, and fission-track analysis and He dating from apatite by Gray et al. (2001).

\*FIGURE 5\*

Hooker et al. (2015) concluded that set B fractures formed during maximum burial, based on the greatest- $T_h$  fluid inclusions within synkinematic cements of that set and also relatively high-strain twins in postkinematic carbonate cements that pre-date set C. Hooker et al. (2015) also concluded that Set C formed amid gradually cooling temperatures, consistent with (i) the regional burial history model of Gray et al. (2001), which shows a simple burial-exhumation trend that lacks major perturbations in time-temperature space (Fig. 5D), and (ii) lower- $T_h$  fluid inclusions in later synkinematic cements within a Set C macrofracture (fracture C5, Figure 6).

\*FIGURE 6\*

Recognizing this observed trend between temporal sequence and cooling  $T_h$ , we can use  $T_h$  as a proxy for opening time for fractures within Set C. In principle,  $T_h$  represents a minimum estimate of the true temperature at which the inclusion formed, called the trapping temperature ( $T_t$ ) (Goldstein and Reynolds, 1994). The difference between  $T_t$  and  $T_h$  depends on the fluid pressure at the time of trapping (Goldstein and Reynolds, 1994; Steele-MacInnis et al., 2012). The appropriate pressure correction for Set C is unknown (Hooker et al., 2015); however, it was argued in that study, on the basis of progressive increasing salinity among fractures underlying an evaporitic décollement, that major increases of fluid pressure were unlikely. Without major temporal changes in fluid pressure, we can attribute differences in  $T_h$  to differences in temperature and therefore time, during exhumation-related cooling (Fig. 5D).

From the scanline measured in the field, using a hand lens, a sample was selected for fluid inclusion analysis of a single macrofracture (C10) and any microfractures detected using SEM. One hundred such microfractures were detected, 31 of which contain analyzable fluid inclusions (Figure 6).

Within both macro- and microfractures, both single-phase and dual-phase (liquid and vapor) fluid inclusions are present (Figure 7).  $T_h$  was measured for all dual-phase fluid inclusions. Most fluid inclusions are present in assemblages, i.e. planes running parallel to fracture walls. Such assemblages coincide with crack-seal increments visible in CL within quartz crystals. Inclusions within an assemblage are interpreted to have formed contemporaneously, ideally preserving the same  $T_h$ . However, intra-assemblage  $T_h$  was observed to range by an average of 21.9°C. Hooker et al. (2015) interpreted this variation to result from short-term fluctuations in temperature, pressure, or salinity during synkinematic cementation. All observed microfractures are entirely sealed by quartz, whereas both macrofractures include synkinematic quartz cements and postkinematic calcite.

With the goal of detecting any change in temperature, and therefore timing, between macrofractures and microfractures, we compared the measured  $T_h$  values between the two fracture size-ranges in two ways. First, we compiled all data, weighting each  $T_h$  value equally. Second, we included only median  $T_h$  values from individual fluid inclusion assemblages. In doing so we also removed all measurements of single fluid inclusions. For this second comparison we also removed three  $T_h$  values from microfractures and two from macrofracture C10 which had anomalously high median  $T_h$  values, a variable liquid:vapor ratio, a corroded appearance in plane light, and, in the case of C10, an orientation along a plane lying roughly 30° from the fracture wall (Fig. 7C). The unfiltered and filtered datasets, for the combined microfractures and each macrofracture, are well fit by normal distributions (Figure 8). We compared these distributions of  $T_h$  using  $t$  tests (see e.g., McKillup and Dyar, 2010), with the null hypothesis being no difference in mean  $T_h$  between the microfractures and each macrofracture. The two-tailed  $t$  tests allow rejection of the null hypothesis for macrofracture C10 and the nearby microfractures with >98% confidence, using either the total or median-only

distributions. In all cases, the mean  $T_h$  for the macrofractures is significantly lower than that of the microfractures, although the ranges of the two populations overlap.

\*FIGURE 7\*

\*FIGURE 8\*

## 7. Discussion

Fracture strain related to fracture formation in sandstones appears to accumulate incrementally, as recorded in SEM-CL images of natural fractures, which generally contain crack-seal texture (Figure 1; see also Hooker et al., 2014). It is not clear whether a crack-seal increment necessarily grew in a single discrete opening increment that was subsequently sealed, because each preserved increment could represent multiple smaller opening episodes that were later sealed, or the opening may have been transiently wider, such that the fracture collapsed to the width preserved by cement precipitation. But whatever the details of the process of fracture opening, the preserved record is one of arrays of fractures, each of which enlarged in discrete steps.

Previous work has shown that the opening of individual fractures overlaps temporally with that of other fractures in the same set. Thermal-history modeling of fracture opening (Becker et al., 2010; Fall et al., 2015; Hooker et al., 2015) is consistent with protracted opening histories of individual fractures, precluding the interpretation that fractures in a set open one at a time. As well, a survey of the isotopic compositions and fluid inclusions of fractures within a set in northeastern Mexico showed that large populations of calcite veins formed amid the same fluid conditions (Smith et al., 2014), suggesting a coeval, rather than sequential, formation.

Based on these previous works, we assume that fractures within the sets we surveyed generally opened coevally. Furthermore, based on our spacing data, we believe that, with increasing strain,

fracture spatial arrangements evolve from indistinguishable-from-random to strongly clustered. In a strongly clustered pattern, fracture abundance in the vicinity of extant fractures is statistically high, in contrast to a regularly spaced pattern, in which fractures are scarce near extant fractures. Therefore we conclude from our data that as fractures grow, the presence of a fracture increases the tendency for nearby fractures to grow.

It has previously been argued that regularly spaced patterns result from extant fractures suppressing the growth of nearby fractures. For example, Rives et al. (1992) described the evolution of a layerbound, regularly spaced fracture pattern as initially random and featuring an exponential distribution, progressing toward a log-normal distribution as fractures began to halt one another's growth via the stress relief in their lateral vicinities, and finally to a normal distribution as a regular fracture spacing developed. We likewise infer that microfracture sets undergo a transition from a pattern well described by an exponential distribution to one well described by a log-normal distribution, based on the  $\chi^2$  test results for sets with varying average fracture spacing (Fig. 3B). However, in the present case, the best-fit log-normal distributions have high standard deviations, reflected in the high  $C_v$  values (Fig. 3B), and indicating clustered fracture patterns.

What remains to be explained is why some growing fractures induce nearby fracture growth (this study) and some suppress it (Rives et al., 1992). Two important differences between those two cases are that the fracture sets in this study (i) are generally not layerbound (Table 1, Figure 2), and (ii) opened amid cement precipitation. In the next two subsections we discuss potential ramifications of these two differences.

#### 7.1. Growth of fractures in mechanically stratified versus isotropic rock

The presence of height-restricting strata allows for a simplified geometrical treatment of the spacing of parallel fractures, in that relatively little propagation is required before a fracture reaches its

maximum height. In such a case the perturbation of the stress field within the host bed is dominated by fracture-lateral stress relief (Rives et al., 1992; Schöpfer et al., 2011).

For fractures that are not layerbound, stress concentration near the fracture tips is comparatively important for the development of nearby fractures. It has been observed, here and previously, that fracture tips and traces are not continuous but rather are segmented (e.g., Segall and Pollard, 1983; Gudmundsson, 1987; Foxford et al., 2000; Philipp, 2012; Arndt et al., 2014). A likely reason for segmentation of a propagating, opening-mode crack is that the loading of such a crack by a remote tensile stress will produce a region of enhanced tension in the vicinity of the crack tip (e.g., Pollard and Segall, 1987). For subcritically stressed fractures, which may propagate over geological time scales, this enhanced tension will promote the propagation of nearby microfractures (Olson, 1993).

Consequently, when the tip of a propagating fracture approaches a particularly well oriented flaw or microcrack, that microcrack will propagate at the expense of the original fracture, potentially halting it. Olson (1993) used a numerical model to show that such a mechanism can produce highly clustered fracture patterns, depending on rock mechanical properties and the initial flaw distribution, even using a stratabound geometry. For a population of subcritically propagating fractures in the absence of stratigraphic boundaries, we might therefore expect a clustered spatial arrangement.

## 7.2. Fracture growth during concomitant mineral cementation

That the fractures we studied opened amid cement precipitation implies that fluids filled the fractures as they grew. The dynamics of fracture interaction will depend in part on the driving mechanism of the fractures, that is, whether the fractures were forced open by increases in fluid pressure or decreases in remote stress. The aforementioned relief of tensile stress adjacent to existing fractures applies to fractures driven by remote extension (Engelder and Fischer, 1996) and could likewise result from fluid-driven fracturing amid a constant confining stress (Fischer et al., 1995). In both cases, the tensile relief is the result of strain-energy minimization in the host rock during fracturing.

However, Engelder and Fischer (1996) also point out that the elastic strain energy within the rock can actually increase as a result of fluid driven fracturing, depending on the coupling between fluid pressure, fracture opening, and confining stresses. For example, a fracture cluster might potentially develop in a laterally confined rock volume into which fluid is injected at a point source, such as a reservoir-breaching fault (Mourgues et al., 2011). Such a geometry might produce cross-stratal clustering of fractures, which, as stated above, would be difficult to recognize in our data because our method samples fractures along bedding.

Cementation of fractures during their opening might also contribute to fracture clustering. For example, if a propagating fracture triggers new microcracks to open by virtue of the enhanced tension near its tip, we might nonetheless expect those microcracks to close if the tip of the parent crack continues to propagate, in which case those microcracks would fall within the region of relaxed tension lateral to the parent crack. However, if fracture growth were slow compared to cementation, microcracks might become cemented, inhibiting closure (Cosgrove, 2001; Laubach et al., 2004).

Furthermore, the development of crack-seal texture within fractures suggests that what is interpreted as a single fracture that is, a single parting of the original host rock, is really an amalgamation of multiple ruptures. What appear to be individual examples of such ruptures, based on homogeneous cement fill, commonly extend across multiple grains (Fig. 1A–D). If regions of enhanced tension near the tips of these ruptures could promote the opening of cracks nearby, then clusters of microfractures could potentially develop in regions beside larger fractures that would otherwise be expected to have relaxed tension. In this context, Hooker and Katz (2015) used a numerical model simulating extending layered rock to show that fracture spacing decreases as the rate of rebonding of fractures via cementation increases.

### 7.3. Clustering of fractures in the Huizachal Group

For most fractures in our dataset we have little constraint on the driving mechanism of fracture opening. The fractures are present in parallel sets and their strain generally reflects the degree of tectonic deformation, pointing to an importance of remotely applied tectonic stresses. Nevertheless, the fractures were synkinematically filled by cement, and thus formed in the subsurface under some fluid pressure, whether hydrostatic or greater. Therefore they were likely driven open by some combination of increases in fluid pressure and decreases in remote compression, with other drivers perhaps active as well.

However, for the Huizachal Group fractures it was argued (Hooker et al., 2015) that fracturing proceeded amid descending fluid and therefore that decreases in remote compression were more important than increases in fluid pressure. This conclusion argues against the possibility of fracture clustering owing to local fluid injection, and the generally non-stratabound arrangement of these fractures argues against mechanical stratigraphy exerting an important control on fracture spacing.

The macrofractures in the Huizachal Group contain fluid inclusions that homogenize at temperatures equal to or lower than those within the microfractures. We therefore interpret that the opening history of the macrofractures coincided with and post-dated that of the microfractures. It may be that the microfractures formed within the zone of increased stress near propagating macrofracture tips, as suggested by Delaney et al. (1986) for barren fractures in the vicinity of magmatic dykes. In the present case, the microfractures and macrofractures alike are cemented, presumably reflecting cement precipitation rates that are limited by crystal-growth kinetics (Lander and Laubach, 2015) rather than influx of filling material, as would be the case for magmatic dykes.

It is also evident that the macrofractures were not completely sealed by quartz, because postkinematic calcite overlaps quartz deposits; in contrast, smaller fractures are commonly entirely sealed by quartz during fracture opening. During fracture growth, new fracturing increments may have been preferentially localized upon the partially sealed macrofracture as opposed to the entirely sealed microfractures, owing to greater adhesion across more thoroughly sealed fractures. If true, a greater

susceptibility to further opening among the largest, most porous fractures could create a positive feedback loop between fracture size, porosity, and susceptibility to re-opening, such that future opening increments are preferentially localized upon the largest few fractures (Hooker et al., 2012).

In some rare examples, cooler  $T_h$  was measured within microfractures clustered around macrofracture C10 (Figure 6). These results could be statistical anomalies, or could reflect imperfect localization of later strain increments upon large, open fractures, leading to clustering as discussed above.

Regardless, the bulk of the evidence supports an initially diffuse pattern of fracture opening becoming progressively focused with time and strain.

Finally, we note that if natural fractures open over millions of years (Becker et al., 2010; Hooker et al., 2015; Lander and Laubach, 2015), then creep processes could dissipate near-fracture stress-field perturbations. In an extreme position on a hypothetical spectrum, in which creep is fast compared to fracture opening, such near-fracture stresses could be effectively dissipated before the next fracture-increment forms, leading to a random fracture pattern. Where the effects of creep are more moderate, we may expect the muting of stress-field perturbations, increasing the relative importance of cement adhesion for fracture spacing. Accordingly, it was shown by Alzayer et al. (2015) that fracture propagation and widening are slow and possibly temporally distinct processes that involve both elastic and inelastic deformations.

## 8. Conclusions

A survey of sandstone microfracture spacings from a range of formations and structural settings shows that natural microfractures are not regularly spaced. Rather, low-strain fracture sets have spatial distributions that are indistinguishable from random, whereas high-strain sets are systematically clustered. In a representative example from the Huizachal Group in northeastern Mexico, fluid-inclusion temperatures combined with burial history modeling suggest that large fractures are age-equivalent to, or post-date, nearby microfractures. We suggest that systematic clustering of fractures

could result from dynamic fracture interaction during propagation, from synkinematic cementation of fractures, and by dissipation of near-fracture stresses by creep processes during fracture growth.

## Acknowledgments

This study was funded in part by grant DE-FG02-03ER15430 from Chemical Sciences, Geosciences and Biosciences Division, Office of Basic Energy Sciences, Office of Science, U.S. Department of Energy, by the GDL Foundation (field work), by the Fracture Research and Application Consortium, and by the Geology Foundation of the Jackson School of Geosciences, The University of Texas at Austin. We thank Hyein Ahn and Karen Black for SEM imaging, Peter Eichhubl, András Fall, Julia Gale, and Leonel Gomez for valuable discussions, and William Dunne, Kei Ogata, and Hannah Watkins for critical reviews.

## References

- Alzayer, Y., Eichhubl, P., Laubach, S.E., 2015. Non-linear growth kinematics of opening-mode fractures. *Journal of Structural Geology* 74, 31–44, doi: 10.1016/j.jsg.2015.02.003.
- Anders, M.H., Laubach, S.E., Scholz, C.H., 2014. Microfractures: a review. *Journal of Structural Geology* 69 (B), 377–394, doi: 10.1016/j.jsg.2014.05.011.
- Arndt, M., Virgo, S., Cox, S.F., Urai, J.L., 2014. Changes in fluid pathways in a calcite vein mesh (Natih Formation, Oman Mountains): insights from stable isotopes. *Geofluids* 14, 391–418.
- Becker, S.P., Eichhubl, P., Laubach, S.E., Reed, R.M., Lander, R.H., Bodnar, R.J., 2010. A 48 m.y. history of fracture opening, temperature, and fluid pressure: Cretaceous Travis Peak Formation, East Texas basin. *GSA Bulletin* 122 (7/8), 1081–1093.

Cosgrove, J.W., 2001. Hydraulic fracturing during the formation and deformation of a basin: A factor in the dewatering of low-permeability sediments. *AAPG Bulletin* 85 (4), 737–748.

Delaney, P. T., Pollard, D. D., Ziony, J. I., McKee, E. H., 1986. Field relations between dikes and joints: emplacement processes and paleostress analysis. *Journal of Geophysical Research: Solid Earth*, 91(B5), 4920–4938.

Engelder, T., Fischer, M. P., 1996. Loading configurations and driving mechanisms for joints based on the Griffith energy-balance concept. *Tectonophysics* 256 (1-4), 253–277.

Fall, A., Eichhubl, P., Bodnar, R.J., Laubach, S.E., Davis, J.S., 2015. Natural hydraulic fracturing of tight-gas sandstone reservoirs, Piceance Basin, Colorado. *GSA Bulletin* 127 (1/2), 61–75.  
doi:10.1130/B31021.1.

Fischer, M. P., Gross, M. R., Engelder, T., Greenfield, R. J., 1995. Finite-element analysis of the stress distribution around a pressurized crack in a layered elastic medium: implications for the spacing of fluid-driven joints in bedded sedimentary rock. *Tectonophysics* 247 (1), 49–64.

Foxford, K.A., Nicholson, R., Polya, D.A., Hebblethwaite, R.P.B., 2000. Extensional failure and hydraulic valving at Minas da Panasqueira, Portugal: evidence from vein spatial distributions, displacements and geometries. *Journal of Structural Geology* 22, 1065–1086.

Gillespie, P.A., Johnston, J.D., Loriga, M.A., McCaffrey, K.J.W., Walsh, J.J., Watterson, J., 1999. Influence of layering on vein systematics in line samples. In: McCaffrey, K.J.W., Walsh, J.J., and Watterson, J., eds., *Fractures, Fluid Flow, and Mineralization*. Geological Society [London] Special Publication 155, 35–56.

- Giorgioni, M., Iannace, A., D'Amore, M., Dati, F., Galluccio, L., Guerriero, V., Mazzoli, S., Parente, M., Strauss, Vitale, S., 2016. Impact of early dolomitization on multi-scale petrophysical heterogeneities and fracture intensity of low-porosity platform carbonates (Albian–Cenomanian, southern Apennines, Italy). *Marine and Petroleum Geology* 73, 462–478.
- Goldstein, R.H., Reynolds, T.J. 1994. *Systematics of Fluid Inclusions in Diagenetic Minerals*. Tulsa: SEPM Short Course Notes 31, 199 p.
- Gomez, L.A., Laubach, S.E., 2006. Rapid digital quantification of microfracture populations. *Journal of Structural Geology* 28, 408–420.
- Gray, G.G., Pottorf, R.J., Yurewicz, D.A., Mahon, K.I., Pevear, D.R., Chuchla, R.J., 2001. Thermal and chronological record of syn- to post-Laramide burial and exhumation, Sierra Madre Oriental, Mexico. In: Bartolini, C., Buffler, R.T., and Cantú-Chapa, A., eds., *The western Gulf of Mexico Basin: Tectonics, sedimentary basins, and petroleum systems: AAPG Memoir* 75, 159–181.
- Griffith, A. A., 1921. The phenomena of rupture and flow in solids. *Philosophical Transactions of the Royal Society of London. Series A, containing papers of a mathematical or physical character*, 221, 163–198.
- Gudmundsson, A., 1987. Geometry, formation and development of tectonic fractures on the Reykjanes Peninsula, southwest Iceland. *Tectonophysics* 139, 295–308.
- Helgeson, D. E., Aydin, A., 1991. Characteristics of joint propagation across layer interfaces in sedimentary rocks. *Journal of Structural Geology* 13 (8), 897–911.
- Hooker, J.N., Gomez, L.A., Laubach, S.E., Gale, J.F.W., Marrett, R., 2012. Effects of diagenesis (cement precipitation) during fracture opening on fracture aperture-size scaling in carbonate rocks. In:

- Garland, J., Neilson, J.E., Laubach, S.E., and Whidden, K.J., eds., *Advances in Carbonate Exploration and Reservoir Analysis*. Geological Society [London] Special Publication 370, 187–206.
- Hooker, J.N., Katz, R.F., 2015. Vein spacing in extending, layered rock: the effect of synkinematic cementation. *American Journal of Science* 315, 557–588.
- Hooker, J.N., Larson, T.E., Eakin, A., Laubach, S.E., Eichhubl, P., Fall, A., Marrett, R., 2015. Fracturing and fluid flow in a sub-décollement sandstone; or, a leak in the basement. *Journal of the Geological Society* 172, 428–442.
- Hooker, J.N., Laubach, S.E., Marrett, R., 2013. Fracture-aperture size—frequency, spatial distribution, and growth processes in strata-bounded and non-strata-bounded fractures, Cambrian Mesón Group, NW Argentina. *Journal of Structural Geology* 54, 54–71.
- Hooker, J.N., Laubach, S.E., Marrett, R., 2014. A universal power-law scaling exponent for fracture apertures in sandstones. *GSA Bulletin* 126 (9/10), 1340–1362.
- Kuiper, N.H., 1960. Tests concerning random points on a circle. *Proceedings of the Koninklijke Nederlandse Akademie van Wetenschappen (A)* 63, 38–47.
- Ladeira, F. L., and Price, N. J., 1981. Relationship between fracture spacing and bed thickness. *Journal of Structural Geology* 3 (2), 179–183.
- Lander, R.H., Laubach, S.E., 2015. Insights into rates of fracture growth and sealing from a model for quartz cementation in fractured sandstones. *GSA Bulletin* 127 (3/4), 516–538.
- Laubach, S.E., 1997. A method to detect natural fracture strike in sandstones. *AAPG Bulletin* 81, 604–623.

- Laubach, S.E., Olson, J.E., Gale, J.F.W., 2004. Are open fractures necessarily aligned with maximum horizontal stress? *Earth and Planetary Science Letters* 222, 191–195.
- Laubach, S.E., Ward, M.E., 2006. Diagenesis in porosity evolution of opening-mode fractures, Middle Triassic to Lower Jurassic La Boca Formation, NE Mexico. *Tectonophysics* 419, 75–97.
- McKillop, S., Dyar, M.D., 2010. *Geostatistics Explained: An Introductory Guide for Earth Scientists*. Cambridge: Cambridge University Press, 396 p.
- Mourgues, R., Gressier, J. B., Bodet, L., Bureau, D., Gay, A., 2011. “Basin scale” versus “localized” pore pressure/stress coupling—Implications for trap integrity evaluation. *Marine and Petroleum Geology* 28 (5), 1111–1121.
- Narr, W., 1996. Estimating average fracture spacing in subsurface rock. *AAPG Bulletin* 80 (10), 1565–1586.
- Narr, W., Suppe, J., 1991. Joint spacing in sedimentary rocks. *Journal of Structural Geology* 13 (9), 1037–1048.
- Ogata, K., Senger, K., Braathen, A., Tveranger, J., 2014. Fracture corridors as seal-bypass systems in siliciclastic reservoir-cap rock successions: Field-based insights from the Jurassic Entrada Formation (SE Utah, USA). *Journal of Structural Geology* 66, 162–187.
- Ogata, K., Storti, F., Balsamo, F., Tinterri, R., Bedogni, E., Fetter, M., Gomes, L., Hatushika, R., 2016. Sedimentary facies control on mechanical and fracture stratigraphy in turbidites. *GSA Bulletin* 129 (1/2), 76–92.

Olson, J.E., 1993. Joint pattern development: effects of subcritical crack growth and mechanical crack interaction. *Journal of Geophysical Research* 98 (B7), 12,251–12,265.

Philipp, S.L., 2012. Fluid overpressure estimates from the aspect ratios of mineral veins. *Tectonophysics* 581, 35–47.

Pollard, D.D., Segall, P., 1987. Theoretical displacements and stresses near fractures in rock: with applications to faults, joints, veins, dikes, and solution surfaces. In: Atkinson, B.K., ed., *Fracture Mechanics of Rock*. London: Academic Press, 277–349.

Putz, M.W., Sanderson, D.J., 2008. The distribution of faults and fractures and their importance in accommodating extensional strain at Kimmeridge Bay, Dorset, UK. In: Wibberley, C.A.J., Kurz, W., Holdsworth, R.E., and Collettini, C., eds., *The internal structure of fault zones: implications for mechanical and fluid-flow properties*. Geological Society [London] Special Publication 299, 97–111.

Rives, T., Razack, M., Petit, J.-P., Rawnsley, K.D., 1992. Joint spacing: analogue and numerical simulations. *Journal of Structural Geology* 14 (8/9), 925–937.

Savalli, L., Engelder, T., 2005. Mechanisms controlling rupture shape during subcritical growth of joints in layered rocks. *Geological Society of America Bulletin* 117 (3–4), 436–449.

Schöpfer, M.P.J., Arslan, A., Walsh, J.W., Childs, C., 2011. Reconciliation of contrasting theories for fracture spacing in layered rocks. *Journal of Structural Geology* 33, 551–565.

Segall, P., Pollard, D.D., 1983. Joint formation in granitic rock of the Sierra Nevada. *GSA Bulletin* 94, 563–575.

Smith, A.P., Fischer, M.P., Evans, M.A., 2014. On the homogeneity of fluids forming bedding-parallel veins. *Geofluids* 14, 45–57.

Steele-MacInnis, M., Lecumberri-Sanchez, P., Bodnar, R.J., 2012. HOKIEFLINCS\_H2O-NaCl: A Microsoft Excel spreadsheet for interpreting microthermometric data from fluid inclusions based on the PVTX properties of H<sub>2</sub>O–NaCl. *Computers & Geosciences* 49, 334–337.

Stephens, M.A., 1965. The goodness-of-fit statistic  $V_N$ : distribution and significance points. *Biometrika* 52 (3/4), 309–321.

Sterner, S.M., Bodnar, R.J., 1984. Synthetic fluid inclusions in natural quartz I. Compositional types synthesized and applications to experimental geochemistry. *Geochimica et Cosmochimica Acta* 48, 2659–2668.

Tang, C. A., Z. Z. Liang, Y. B. Zhang, X. Chang, X. Tao, D. G. Wang, J. X. Zhang, J. S. Liu, W. C. Zhu, D. Elsworth, 2008. Fracture spacing in layered materials: a new explanation based on two-dimensional failure process modeling. *American Journal of Science* 308 (1), 49–72.

## Figure captions

Figure 1. Natural fractures in sandstones. TM: transgranular microfracture; IM: intragranular microfracture; E: epoxy; FW: fracture wall; Cal: calcite; Qtz: quartz. (A) SEM-CL image, Sample 44. Bright-luminescing, epoxy-filled fractures are artificial and caused during sample preparation. Transgranular microfractures are interpreted to post-date deposition, whereas intragranular microfractures might have been inherited within the grains. Nonetheless, grain-scale effects likely affect fracture propagation; at arrow 1, a transgranular microfracture deflects along grain boundaries. Fractures are commonly segmented (arrow 2), including septae of host rock whose size varies by the stepping distance and degree of linkage between the segments. (B) SEM-CL image, Sample 44.

Macrofracture filled by quartz and calcite cements. Quartz cement is interpreted as synkinematic by virtue of crack-seal texture, with cracking increments running parallel to fracture walls. Calcite cement is mostly free of crack-seal texture and overlaps quartz, and so is interpreted as postkinematic. (C) SEM-CL image, Sample 2. Quartz-sealed, transgranular microfractures tend to splay into separate segments that otherwise, in size and orientation with respect to larger fractures, resemble the crack-seal segments in (B). Such splaying is interpreted as imperfect localization of crack-seal growth; see text for discussion. (D) SEM-CL image, Sample 53. Microfractures are entirely sealed by quartz whereas wider macrofracture contains some porosity, marked by dashed lines. (E) Field photograph, Huizachal Group, northeastern Mexico. Two quartz-bearing fracture sets are present. Arrow 3 marks a link between segments within a fracture of the older, crosscut set.

Figure 2. Two-dimensional fracture survey. (A) SEM-CL fracture map, Sample 53. (B) Interpretation of (A), with four-point polygons digitized over fractures representing fracture tips and locations of maximum aperture. (C) Aperture versus length from measurements in (B); log-log scale. The longest fracture measurements are censored owing to the largest fractures transcending the map boundaries.

Figure 3. Microfracture spacing irregularity. (A)  $C_v$  versus number of fractures measured. 95% confidence intervals for  $C_v$  values plotted, measured from repeated random-spacing simulated datasets. For more clustered datasets, the  $\chi^2$  test allows rejection of the exponential distribution, which would be expected for random fracture spacing. (B)  $C_v$  versus number of fractures, normalized by the scanline length. “Clustered” and “Random” refer to each dataset’s position with respect to the regions in (A). Better correlation in (B) versus that in (A) suggests that fracture sets become more clustered as spacing decreases.

Figure 4. Microfracture strain irregularity. (A) Plot of cumulative fracture aperture—that is, the sum of all apertures intersected up to the present fracture—along a scanline, to illustrate  $V'$ . Line of homogeneous strain connects the origin to the cumulative aperture at the end of the scanline.  $D_{\max}$  and  $D_{\min}$  are the maximum and minimum difference, respectively, between the cumulative aperture and

the homogeneous strain line.  $V'$  is calculated as shown and quantifies the heterogeneity of the strain distribution, from 0 (perfectly homogeneous strain) to 1 (maximum possible heterogeneity). (B)  $V'$  versus number of fractures. Symbols as in Figure 3A. Regions statistically distinct from random are delineated using tables from Stephens (1965). A poor correlation exists, which is also the case between  $V'$  and total strain and scanline length. Absence of correlation likely reflects wide variation in  $V'$  among short-scanline samples, regardless of strain measured. Nonetheless, samples with statistically clustered strain distributions are commonly inconsistent with exponential spacing distributions.

Figure 5. Fractures used for micro-thermometric timing reconstructions, Huizachal Group, northeastern Mexico. (A) Outcrop photograph. Dashed lines correspond to the interpreted sets of Laubach and Ward (2006). Set A, not pictured, strikes N–S. (B) SEM-CL image of Set C microfractures. (C) Location of field area. Canyon-floor exposure lies at 24.70N, 100.09 W. (D) Burial history curve for the Huizachal Group, modified from Gray et al. (2001) and Hooker et al. (2015). Dashed lines emphasize that the true timing for each fracture set is uncertain owing to the unknown pressure correction that should be applied to  $T_h$  measurements, but Set B was interpreted to have formed near maximum burial (Hooker et al., 2015), providing a relative constraint for the timing of the other, crosscutting (Sets C, D) and crosscut (Set A) fracture sets.

Figure 6. Aperture, measured as the distance between fracture walls, and  $T_h$  of fractures in Sample 44 and in a nearby macrofracture (C5) from the same fracture set. Macrofractures have cooler  $T_h$  than microfractures, indicating a partially later timing because this fracture set grew amid decreasing temperature (Figure 5D).

Figure 7. Sample 44 fracture cements. Cal: calcite; Qtz: quartz. All images are plane-polarized light photomicrographs. (A) Macrofracture C10. Abundant twinned calcite cement overlaps synkinematic quartz cement. (B) Typical fluid inclusion assemblages in macro- and microfractures lie parallel to fracture walls; larger inclusions commonly contain vapor bubbles. Arrow 1 marks single-phase

(liquid) inclusion; arrow 2 marks dual-phase (liquid and vapor) inclusion. Image is from macrofracture C10. (C) Example of fluid inclusion assemblages from macrofracture C10 that lie oblique to fracture walls and rarely contain bubbles, possibly owing to their small size.  $T_h$  measured from such fluid inclusion assemblages is commonly high ( $>150^\circ\text{C}$ ) and varies considerably, possibly reflecting post-entrapment damage. Such measurements were omitted from Figure 6.

Figure 8. Best-fit normal distributions to fluid inclusion assemblage-median  $T_h$  measurements from Sample 44 macrofracture C10 and microfractures. A two-tailed  $t$  test rejects an equal mean for the two populations with 98% confidence, meaning that the cooling apparent in Figure 6 is statistically significant.

Table 1. Summary of the microfracture spacing dataset, subdivided by field/core area. Locations of samples from Basin X and Formation X are confidential but are distinct from other sample locations. Microfracture strain calculated as (sum of apertures)/(sum of spacings) measured along scanlines (Gomez and Laubach, 2006).

Table 2. Microfracture spacing statistics. Strain calculated as in Table 1 and in text.  $\chi^2$  error is calculated as the summation  $[(P_{\text{obs}} - P_{\text{mod}})^2 / |P_{\text{mod}}|]$  for all fracture spacings where  $P_{\text{obs}}$  and  $P_{\text{mod}}$  are the observed and modeled cumulative probabilities, respectively, of a given spacing size. Values in bold are the minimum  $\chi^2$  errors (i.e., best fits) for the four distribution equations modeled. Exponential and log-normal distributions for the datasets can be rejected as indicated with 95% confidence using the  $\chi^2$  test. Significance of non-random clustering based on  $V'$  taken from critical-value tables in Stephens (1965).  $V'$  values marked with an asterisk (\*) have statistically homogeneous strain distributions. Significance of non-random clustering based on  $C_v$  taken from numerical simulations of randomly arranged fracture spacings.

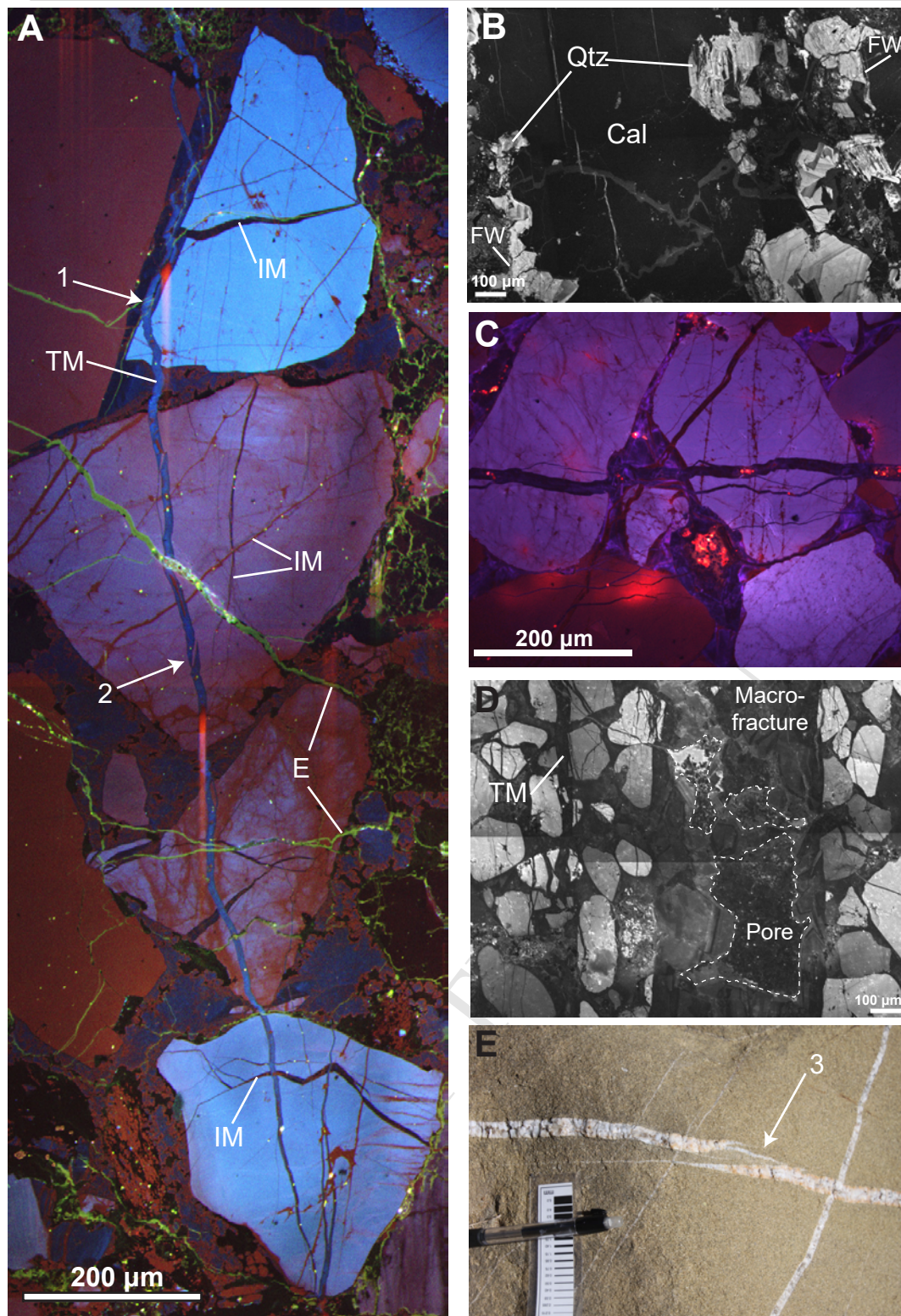
Table 1.

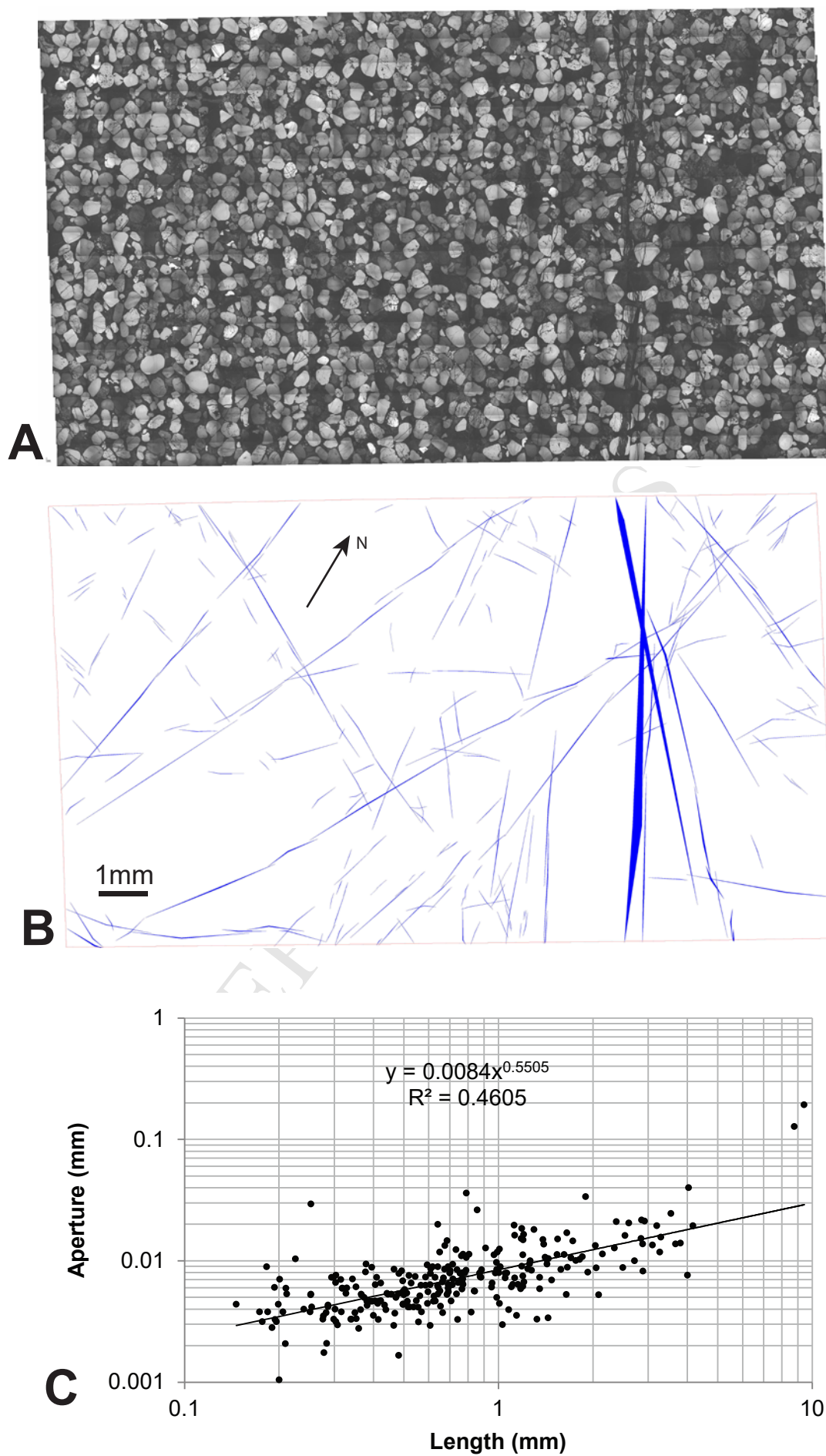
Sample no.	Field area	Location	Formation or Group	Folk classification	Depositional setting	Structural setting	Micro-fracture strain average	Macro-fractures stratabound?	Field or core measurements
1–6	East Texas Basin	Texas, USA	Travis Peak Fm.	Quartzarenite	Marginal-marine	Regional arch	$1.4 \times 10^{-3}$	Yes	Core
7–12	Piceance Basin	Colorado, USA	Mesaverde Gp.	Sub-litharenite, litharenite	Marginal-marine	Regional arch	$4.7 \times 10^{-3}$	Yes	Core
13–40	Basin X	(Confidential)	Formation X	Sub-litharenite	Deltaic-marine	Fold-thrust belt	$1.4 \times 10^{-2}$	No	Core
41–44	Mexican Sierra Madre Oriental	Nuevo León, Mexico	Huizachal Gp.	Feldspathic litharenite, litharenite	Fluvial	Sub-décollement	$1.6 \times 10^{-2}$	No	Field
45–52	Scottish Highlands	Scotland, UK	Eriboll Fm.	Quartzarenite	Upper shoreface	Sub-thrust belt	$2.6 \times 10^{-2}$	No	Field
53–59	Andean Eastern Cordillera	Jujuy, Argentina	Mesón Gp.	Quartzarenite	Upper shoreface	Fold-thrust belt	$4.8 \times 10^{-2}$	Rarely	Field

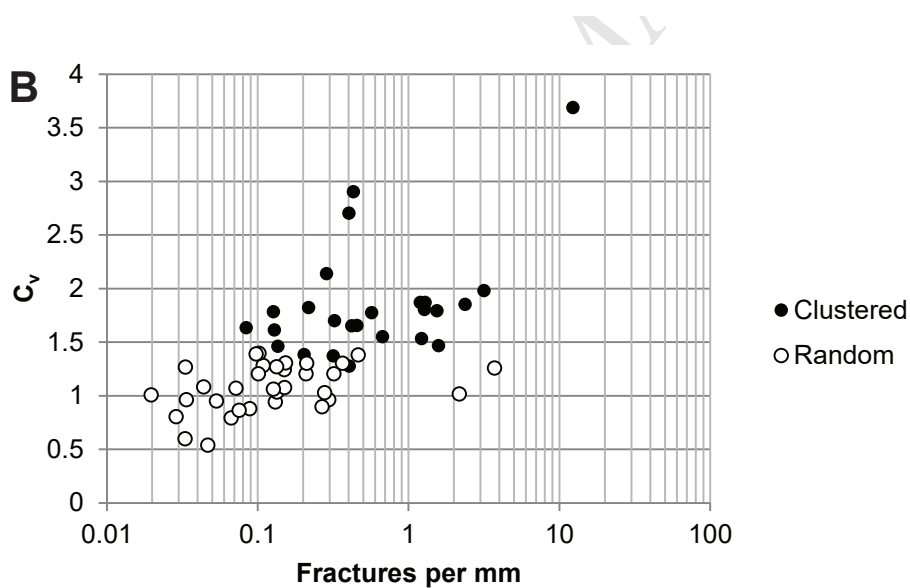
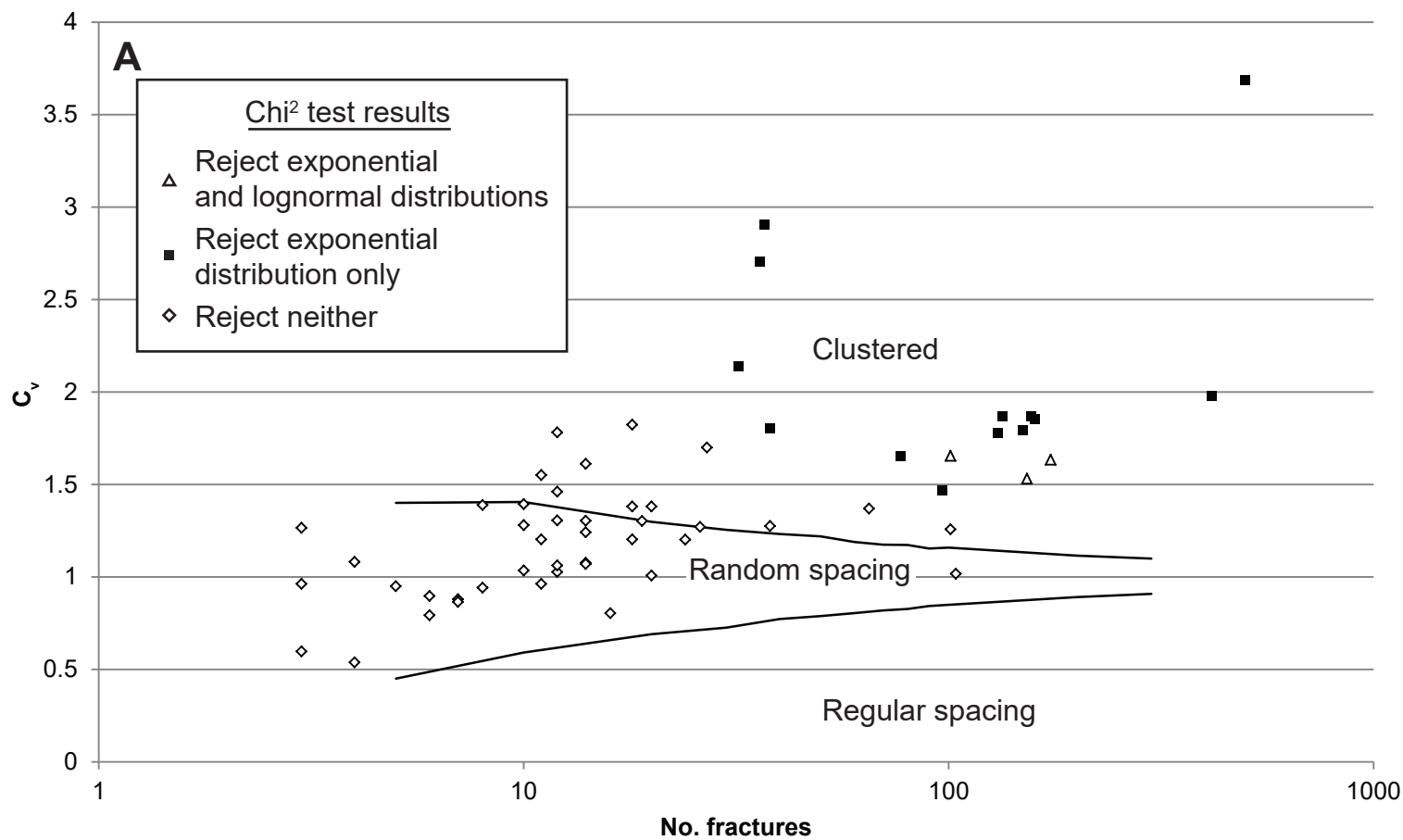
Table 2.

Sample Number	No. micro-fractures	Scanline length (mm)	Strain	Chi <sup>2</sup> error				Reject LN	Reject EXP	V'	V' 95% sig	Cv	Cv 95% sig
				Normal	Log-normal	Power law	Exponential						
1	153	125.3	0.0193	4.6E+05	<b>263.44</b>	2157.14	509.20	X	X	0.41	1	1.53	1
2	38	29.8	0.0088	328.53	<b>10.86</b>	63.17	68.40		X	0.48	1	1.80	1
3	101	27.1	0.0726	2.1E+04	<b>56.36</b>	1262.68	117.74			0.36	1	1.26	1
4	104	47.9	0.0155	343.92	82.47	4700.03	<b>19.39</b>			0.36	1	1.02	0
5	11	37.1	0.0014	3.84	3.63	6.02	<b>1.11</b>			0.33	0	0.96	0
6	11	16.3	0.0357	24.10	2.87	<b>2.35</b>	4.26			0.92	1	1.55	1
7	24	74.8	0.0010	23.30	14.59	22.17	<b>8.47</b>			0.18	0	1.20	0
8	4	90.9	0.0002	1.81	1.76	<b>0.35</b>	0.39			0.47	0	1.08	0
9	12	94.4	0.0009	84.66	<b>4.78</b>	11.31	9.22			0.34	0	1.78	1
10	6	89.7	0.0060	1.92	1.45	0.98	<b>0.19</b>			0.97	1	0.79	0
11	18	82.7	0.0005	164.50	<b>4.55</b>	10.00	14.96			0.34	0	1.82	1
12	3	88.8	0.0001	0.81	1.38	0.31	<b>0.06</b>			0.51	0	0.96	0
13	7	79	0.0039	2.05	4.90	3.54	<b>0.64</b>			0.55	0	0.88	0
14	8	61.1	0.0095	2.03	3.07	2.87	<b>0.69</b>			0.79	1	0.94	0
15	18	86	0.0047	11.55	11.03	14.86	<b>3.15</b>			0.35	0	1.20	0
16	27	83.5	0.0038	88.00	<b>7.88</b>	23.66	27.95			0.57	1	1.70	1
17	10	91.7	0.0048	9.41	4.06	4.54	<b>1.10</b>			0.61	1	1.28	0
18	37	85.6	0.0102	2674.04	<b>11.39</b>	89.88	170.69		X	0.69	1	2.90	1
19	10	74.5	0.0172	4.38	5.19	6.26	<b>1.07</b>			0.46	0	1.03	0
20	5	93.7	0.0007	1.46	2.14	0.82	<b>0.34</b>			0.53	0	0.95	0
21	14	92.9	0.0132	16.27	<b>1.87</b>	9.63	3.25			0.89	1	1.24	0
22	12	78.4	0.0119	18.22	2.83	8.22	<b>2.15</b>			0.88	1	1.31	0
23	3	90.4	0.0008	1.13	1.00	0.20	<b>0.03</b>			0.47	0	1.27	0
24	0	87.3	0										
25	12	88	0.0030	32.31	3.64	5.88	<b>3.30</b>			0.23	0	1.46	1
26	36	89.2	0.0068	1.0E+04	<b>4.96</b>	43.41	141.22		X	0.45	1	2.70	1
27	14	92.6	0.0033	7.50	3.84	12.80	<b>2.01</b>			0.74	1	1.08	0
28	3	90.6	0.0049	1.02	1.25	0.28	<b>0.22</b>			0.42*	0	0.60	0

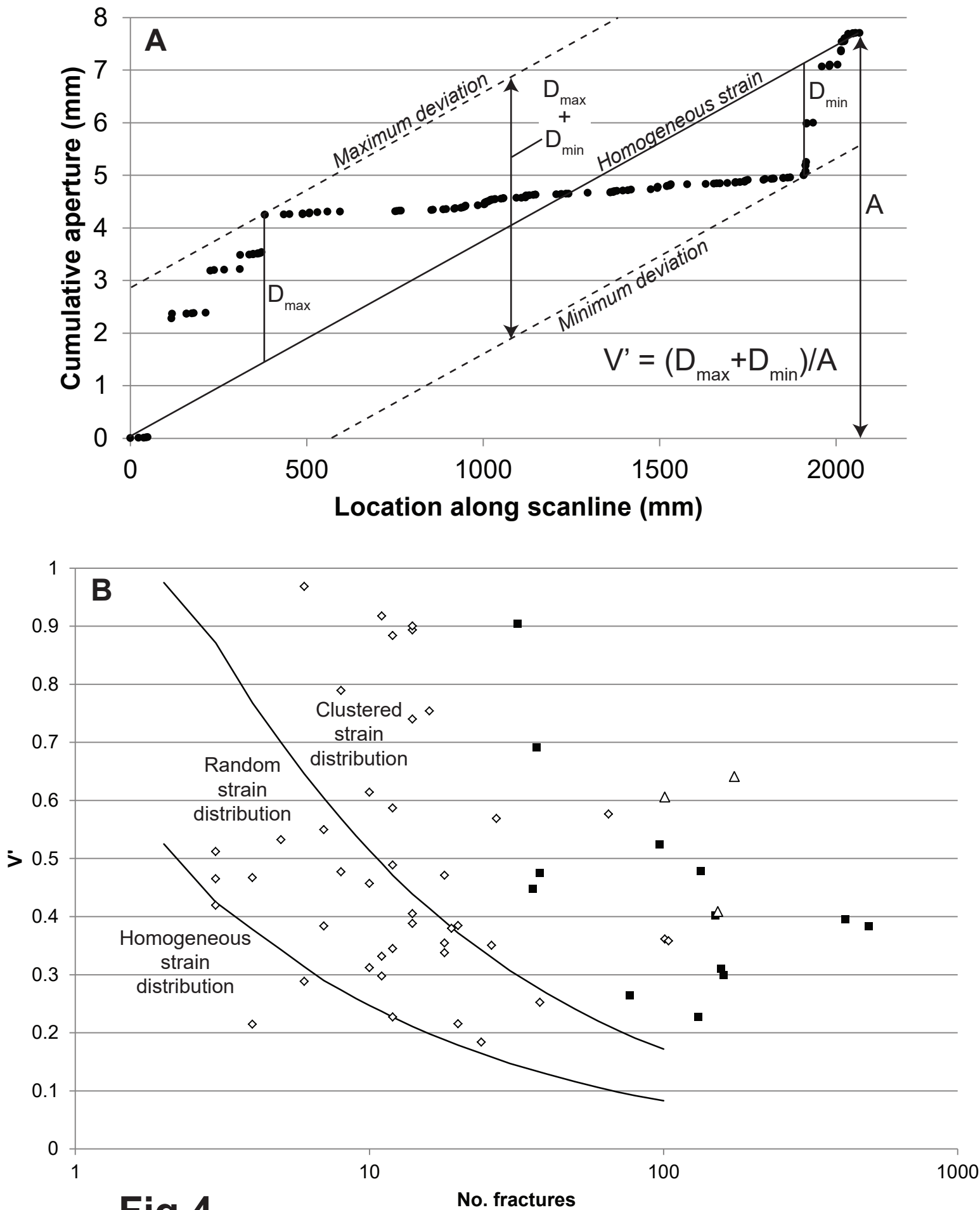
29	14	108.1	0.0002	23.83	<b>3.74</b>	6.49	6.53			0.40	0	1.61	1
30	10	97.6	0.0004	11.91	<b>2.15</b>	5.60	2.35			0.31	0	1.39	0
31	7	92.7	0.0002	1.45	4.81	3.52	<b>0.61</b>			0.38	0	0.86	0
32	20	98.1	0.0007	92.51	<b>4.16</b>	47.23	9.41			0.38	1	1.38	1
33	6	22.4	0.0007	2.11	2.78	2.81	<b>0.74</b>			0.29*	0	0.90	0
34	14	38.3	0.0007	55.14	5.00	15.77	<b>3.50</b>			0.39	0	1.30	0
35	0	20.1	0										
36	18	38.8	0.0061	23.61	<b>5.39</b>	15.68	6.07			0.47	1	1.38	0
37	174	2067.3	0.0034	3.4E+11	<b>1065.15</b>	8571.83	1215.77	X	X	0.64	1	1.63	1
38	32	111.8	0.0209	1063.34	<b>11.34</b>	22.97	75.04		X	0.90	1	2.14	1
39	12	43.2	0.0016	4.40	6.11	9.21	<b>0.79</b>			0.59	1	1.03	0
40	16	554	0.0028	4.39	12.50	28.83	<b>4.07</b>			0.75	1	0.80	0
41	20	1016.7	0.0001	13.11	4.40	29.24	<b>0.91</b>			0.22	0	1.01	0
42	131	229.5	0.0239	5333.42	<b>86.34</b>	754.86	680.44		X	0.23	1	1.77	1
43ew	14	194.7	0.0181	19.89	5.68	21.68	<b>2.15</b>			0.90	1	1.07	0
43ne	26	194.7	0.0015	32.19	15.38	34.17	<b>9.80</b>			0.35	1	1.27	0
44	101	222	0.0091	3.6E+07	<b>127.26</b>	2626.66	6159.98	X	X	0.61	1	1.65	1
45	157	121.6	0.0360	2.2E+08	<b>178.32</b>	1371.79	1105.79		X	0.31	1	1.87	1
46	160	67.5	0.0538	8.0E+08	<b>156.78</b>	1086.42	1148.84		X	0.30	1	1.85	1
47	65	204.6	0.0128	4460.41	71.21	299.77	<b>53.19</b>			0.58	1	1.37	1
48	77	182.8	0.0067	1874.70	<b>72.42</b>	294.65	175.76		X	0.26	1	1.65	1
49	11	108.7	0.0003	7.07	2.42	7.23	<b>1.19</b>			0.30	0	1.20	0
50	12	94.2	0.0006	7.83	4.33	10.18	<b>0.54</b>			0.49	1	1.06	0
51	8	81.6	0.0005	13.58	2.04	<b>0.67</b>	2.29			0.48	0	1.39	0
52	19	89.6	0.0013	111.60	8.18	28.13	<b>7.26</b>			0.38	0	1.30	0
53	134	112.1	0.0359	4.4E+07	<b>55.25</b>	1.2E+04	1973.08		X	0.48	1	1.87	1
54	150	97.1	0.0225	1.4E+04	<b>40.92</b>	1262.72	1013.24		X	0.40	1	1.79	1
55	97	61.4	0.0994	4826.34	<b>45.04</b>	550.73	187.05		X	0.52	1	1.47	1
56	416	131.1	0.1930	1.7E+09	<b>332.77</b>	7288.57	9857.38		X	0.39	1	1.98	1
57	499	40.5	0.0299	4.0E+07	<b>510.28</b>	1.0E+05	1.6E+05		X	0.38	1	3.69	1
58	38	93.7	0.0021	139.00	26.83	99.66	<b>14.04</b>			0.25	0	1.28	1
59	4	85.3	0.0002	2.02	1.96	<b>0.36</b>	0.39			0.21*	0	0.54	0

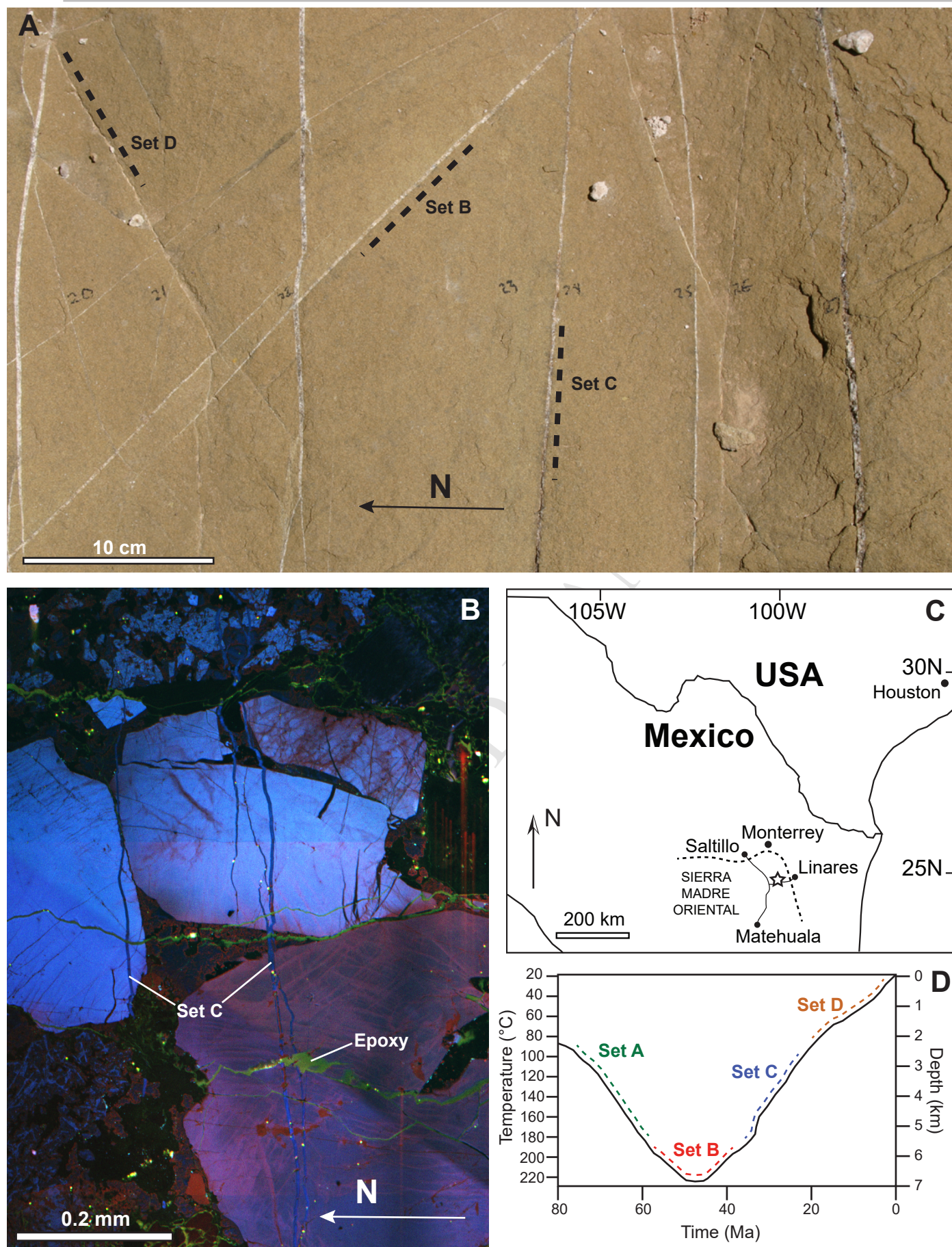
**Fig 1**

**Fig 2**

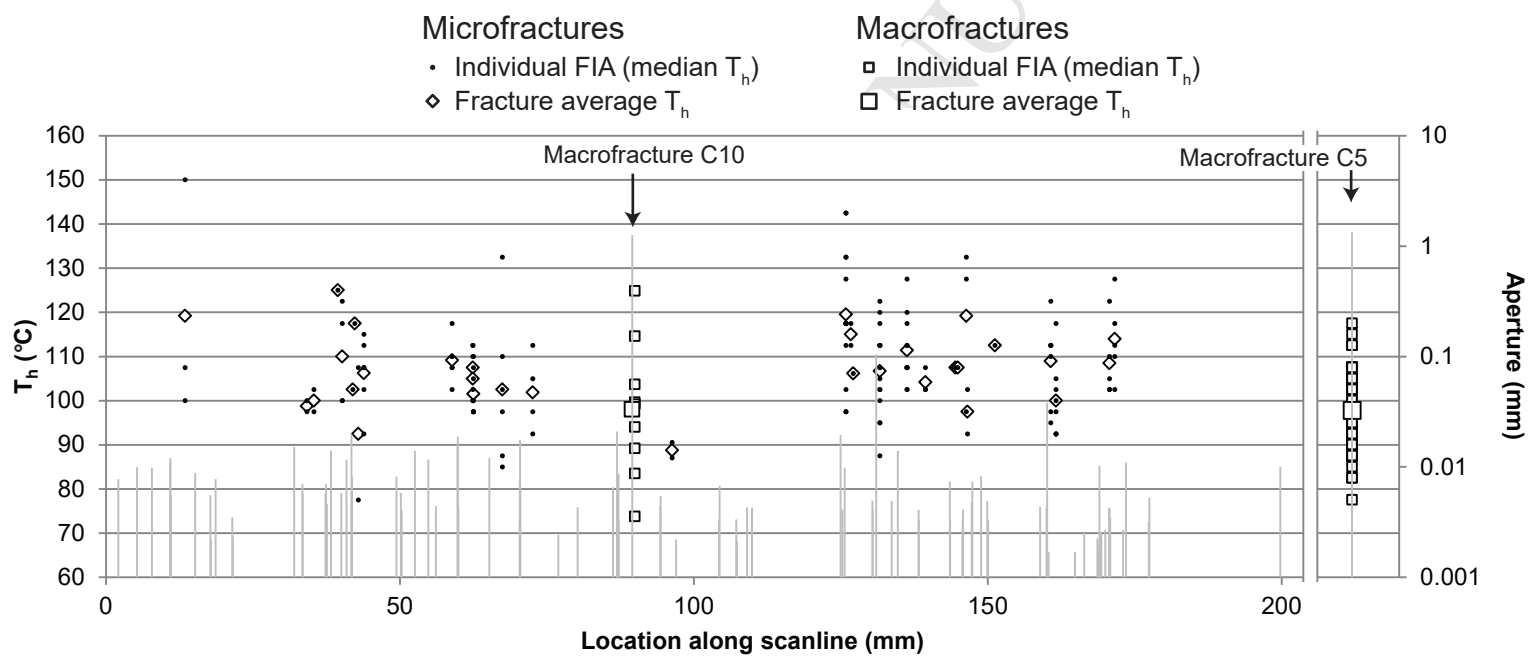


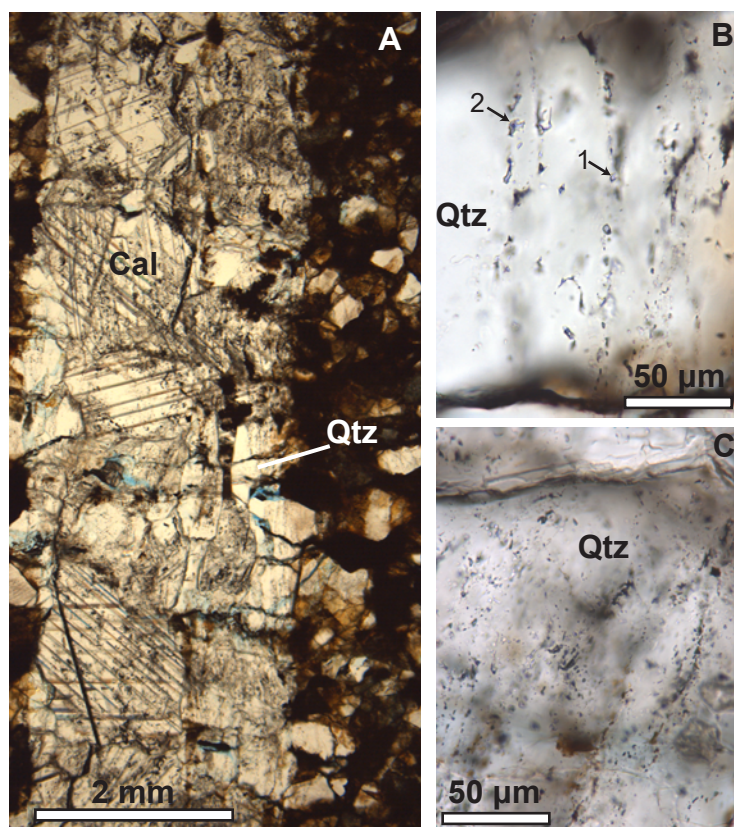
**Fig 3**

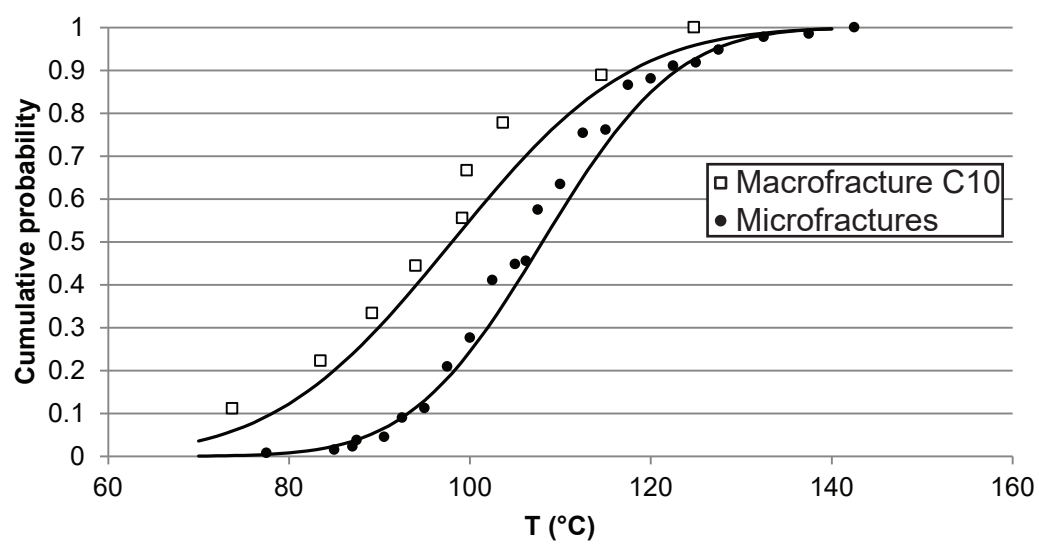
**Fig 4**



**Fig 5**

**Fig 6**

**Fig 7**

**Fig 8**

**Microfracture spacing distributions and the evolution of fracture patterns in sandstones**

J.N. Hooker

S.E. Laubach

R. Marrett

**Highlights**

A survey of microfracture spacings was collected from eight sandstone formations on three continents.

Spacings from low-strain fracture sets are indistinguishable from random.

Spacings from higher-strain fracture sets are systematically clustered.

Fracture opening is progressively focused upon a subset of fractures, whose growth outpaces the rest.

Fracture clustering results from interaction among coevally opening and sealing fractures.